

Article

Role of Diffuser Autocorrelation and Spatial Translation in Computational Ghost Imaging

Yishai Albeck ¹, Shimon Sukholuski ^{2,3}, Orit Herman ², Talya Arusi-Parpar ¹, Sharon Shwartz ⁴ 
and Eliahu Cohen ^{2,*} 

¹ Soreq Nuclear Research Center, Yavne 81800, Israel; yishaial@soreq.gov.il (Y.A.)

² Faculty of Engineering, The Institute of Nanotechnology and Advanced Materials, Bar-Ilan University, Ramat Gan 5290002, Israel

³ Department of Physics, Technion, Haifa 3200003, Israel

⁴ Physics Department, The Institute of Nanotechnology and Advanced Materials, Bar-Ilan University, Ramat Gan 5290002, Israel

* Correspondence: eliahu.cohen@biu.ac.il

Abstract

Ghost imaging (GI) is an imaging modality typically based on correlations between a single-pixel (bucket) detector collecting the electromagnetic field which was transmitted through or reflected from an object and a high-resolution detector which measures the field that did not interact with the object. When using partially coherent sources, fluctuations can be introduced into a beam by rotating or translating a diffuser, and then the beam is split into two beams with identical intensity fluctuations. In computational GI, the diffuser with an unknown scatter distribution is replaced by a diffuser with a known scatter distribution so that the reference beam and high-resolution detector can be discarded. In this work, we wish to examine how the relation between the diffuser's autocorrelation length and its spatial displacement affects the quality of image reconstruction obtained with these methods. We first analyze this general question theoretically and simulatively, and we then present some specific, proof-of-principle results we obtained in an optical setup. Finally, we discuss the relation between theory and experiment, suggesting some general conclusions regarding the preferred working points.



Received: 1 May 2025

Revised: 9 June 2025

Accepted: 23 June 2025

Published: 26 June 2025

Citation: Albeck, Y.; Sukholuski, S.; Herman, O.; Arusi-Parpar, T.; Shwartz, S.; Cohen, E. Role of Diffuser Autocorrelation and Spatial Translation in Computational Ghost Imaging. *Photonics* **2025**, *12*, 650. <https://doi.org/10.3390/photronics12070650>

Copyright: © 2025 by the authors. Licensee MDPI, Basel, Switzerland. This article is an open access article distributed under the terms and conditions of the Creative Commons Attribution (CC BY) license (<https://creativecommons.org/licenses/by/4.0/>).

Keywords: ghost imaging; computational ghost imaging; autocorrelation length; diffuser translation; image reconstruction; total variation minimization

1. Introduction

In 1995, Pittman et al. [1] employed entangled photons produced by parametric downconversion such that the signal interacted with an object before reaching a single-pixel photon-counting detector, while the idler was collected by another single-photon detector. The signal-idler correlations together with the coincidence counting of the two detectors allowed them to reconstruct an image. Later, it was demonstrated by Bennink et al. [2] that a classical source of photons can similarly be used for GI by modulating the beam using a diffuser or some other spatial mask (see also the analysis of Gatti et al. [3]). This way, the quantum mechanical correlations between the entangled signal and idler are replaced by classical spatial correlations. Moreover, Shapiro [4] has shown that the high-resolution detector can be discarded, i.e., it suffices to calculate the propagation of the field of the reference beam without physically measuring it, thereby giving rise to computational GI (CGI). The image is then reconstructed by correlating the calculated field patterns with the

measured intensities at a single pixel detector, as was experimentally demonstrated in [5,6]. These historical developments mark the gradual transition of GI towards simpler, more versatile, readily available setups. Furthermore, indeed, since its first introduction, CGI has found interesting new applications such as remote sensing [7], temporal imaging [8], underwater imaging [9], multi-resolution imaging [10], and multi-spectral imaging [11]. Moreover, the recent use of deep learning techniques has improved the image reconstruction results [12–14], highlighting the quantitative benefits of CGI when combined with robust, modern computational tools.

Therefore, it is CGI which we explore here in theory, simulation, and optical experiment, with the goal of better understanding the physical factors limiting the quality of CGI, as well as presenting simple means to improve its performance. As a prime motivation, we bear in mind the important application of X-ray GI [15–18], which seems to enjoy higher resolution, with potentially less illumination than full-field X-ray imaging. The lack of lenses in X-ray imaging is a distinctive limiting factor which state-of-the-art GI enables to overcome. Hence, in X-ray GI, it is common to use diffusers with fine details to create complex illumination patterns, but the ideal relation between the diffuser's properties and its displacement in each step (or "realization") is not yet clear.

It is possible to realize CGI by either using structured illumination or structured detection, i.e., placing the mask before or after the object, respectively. In our experiment, we chose the latter configuration and tested the relation between the diffuser's translation and autocorrelation length (ACL) on the quality of reconstructed images.

In our scheme we use a diffuser (D) to illuminate an object (x) and accumulate the transmitted (or reflected) radiation in a bucket detector (b). If we measure the transmission of D , we can reconstruct the object x via the bucket detector b and correlation measurements. Using compressed sensing it is possible to decrease the number of measurements by treating the process as a constraint of linear equations and trying to minimize some norms [19–21]. Here we simulate a realistic random diffuser with a certain ACL and investigate how the relation between the diffuser's ACL and displacement influences the image reconstruction.

The rest of the paper is structured as follows. In Section 2, we discuss the basic theoretical considerations in choosing the diffuser's displacement and test them using a simple simulation. In Section 3, we report an experiment we performed to validate these theoretical predictions. Section 4 concludes the work.

2. Heuristic Analysis and Theoretical Results

For simplicity, we assume translation (hereinafter a "jump") in one spatial direction (x direction) over the diffuser. We numerically simulate a diffuser, with an ACL of c pixels, that moves with constant jumps of length l and leads to M illumination instances of an object with a size of $m \times n$ pixels by drawing a $\lceil \frac{m}{c} \rceil \times \lceil \frac{n+l(M-1)}{c} \rceil$ normal random array (mean = 0.5, variance = 0.3) and replacing each element of the array with an array of the size $c \times c$ with the original element repeated inside. This creates a pixelated diffuser. To simulate a realistic diffuser, the absorption needs to be between 0 and 1. The above distribution was chosen in order to simulate a sandpaper diffuser, for instance, one which was previously used in X-ray ghost imaging [22] and X-ray ghost fluoroscopy (GF). However, we could have chosen any kind of distribution and probably achieve similar results (it will be especially apparent below when we represent the diffuser in a matrix form).

Let us investigate the case of jumps, which are integers times the ACL (c). We will concentrate on the 1D case ($m = 1$) for simplicity, but since we can rearrange a 2D object in a 1D form, our discussion will still be valid for such objects. In this case, we get a block matrix as follows:

$$D = \begin{pmatrix} \begin{bmatrix} a_{00} & \cdots & a_{00} \end{bmatrix} & \cdots & \begin{bmatrix} a_{0n} & \cdots & a_{0n} \end{bmatrix} \\ \vdots & \ddots & \vdots \\ \begin{bmatrix} a_{M0} & \cdots & a_{M0} \end{bmatrix} & \cdots & \begin{bmatrix} a_{Mn} & \cdots & a_{Mn} \end{bmatrix} \end{pmatrix}. \tag{1}$$

Our constraints are given by the following:

$$D\vec{x} = \vec{b}. \tag{2}$$

Let us examine now the block form of Equation (2):

$$\tilde{D}\vec{\chi} = \begin{pmatrix} a_{00} & \cdots & a_{0n} \\ \vdots & \ddots & \vdots \\ a_{M0} & \cdots & a_{Mn} \end{pmatrix} \vec{\chi} = \vec{\beta}, \tag{3}$$

where

$$D_{ij} = \tilde{D}_{i \lfloor \frac{i}{c} \rfloor}, x_j = \chi_{\lfloor \frac{j}{c} \rfloor}, b_i = \beta_{\lfloor \frac{i}{c} \rfloor}. \tag{4}$$

A solution for Equation (3) is also a solution for Equation (2) in the sense that every element in χ is repeated in x for c times.

For CGI we use here a common and efficient total variation minimization scheme based on augmented Lagrangian and alternating direction algorithms (TVAL3) [23] which attempts to minimize a Lagrangian of the form

$$\mathcal{L} = \alpha \sqrt{\sum_i \left(\sum_j D_{ij} x_j - b_i \right)^2} + \gamma \sum_j |x_{j+1} - x_j|, \tag{5}$$

where the weights α and γ are typically chosen such that $\alpha \gg \gamma$. This particular choice of scheme was made for simplicity, but the conclusions should be general, as we mainly address the physical rather than computational side of ghost imaging.

The substitutions in Equation (4) naturally fit to the reduction of the norm $|\nabla x|_1 = \sum_j |x_{j+1} - x_j|$ in Equation (4) because they reduce the average gradient. The larger the c is, the more clearly we expect to observe this behavior because the larger the c is, the lower the average gradient is.

A convenient way to reorganize D is by periods, i.e., we can rearrange the rows so that each set of rows has the same block structure as in Equation (1). The higher the number of the set is, the less $|\nabla x|_1$ will cause a block structure as in Equation (3) and the number of such sets is given by $\frac{ACL}{\gcd(ACL, \text{Jump})}$.

With respect to the parameters in our simulation, it theoretically suggests the rough behavior (with larger integers corresponding to a higher chance for a better reconstruction) presented in Table 1.

Furthermore, indeed, we performed many simulative runs reaching the typical results presented in Table 2, whose larger/smaller values accord well with the larger/smaller values in Table 1, thus successfully putting to test the hypothesized behavior of image reconstruction. Table 2 corresponds to a TVAL3 reconstruction of the cameraman image with compression ratio of 20. Some specific examples of the reconstructions we obtained for $ACL = 13$ are given in Figure 1.

Table 1. Fraction $\frac{ACL}{\gcd(ACL, Jump)}$ for several choices of ACL and jump. These numbers are meant to indicate the trend we are expecting to see in the simulative data and experiment, i.e., larger values here predict a better image reconstruction quality.

ACL	Jump							
	2	4	7	13	27	40	70	100
2	1	1	2	2	2	1	1	1
4	2	1	4	4	4	1	2	1
7	7	7	1	7	7	7	1	7
10	5	5	10	10	10	1	1	1
13	13	13	13	1	13	13	13	13
20	10	5	20	20	20	1	2	1

Table 2. Simulative data. The peak signal-to-noise ratio (PSNR) of the TVAL3-reconstructed grayscale cameraman image with a compression ratio of 20. Each value in the table was obtained as the mean of 100 simulations.

ACL	Jump							
	2	4	7	13	27	40	70	100
2	14.2	16.1	17.0	17.0	17.0	16.8	16.8	16.8
4	14.3	18.5	18.8	18.7	18.7	19.2	18.6	19.2
7	14.9	19.5	20.2	20.2	20.2	21.2	21.2	21.2
10	20.3	20.6	20.2	20.2	20.3	18.6	18.6	18.6
13	19.8	19.9	20.0	17.9	20.0	20.0	20.0	20.0
20	19.0	18.7	19.1	19.1	19.1	17.1	17.9	17.1

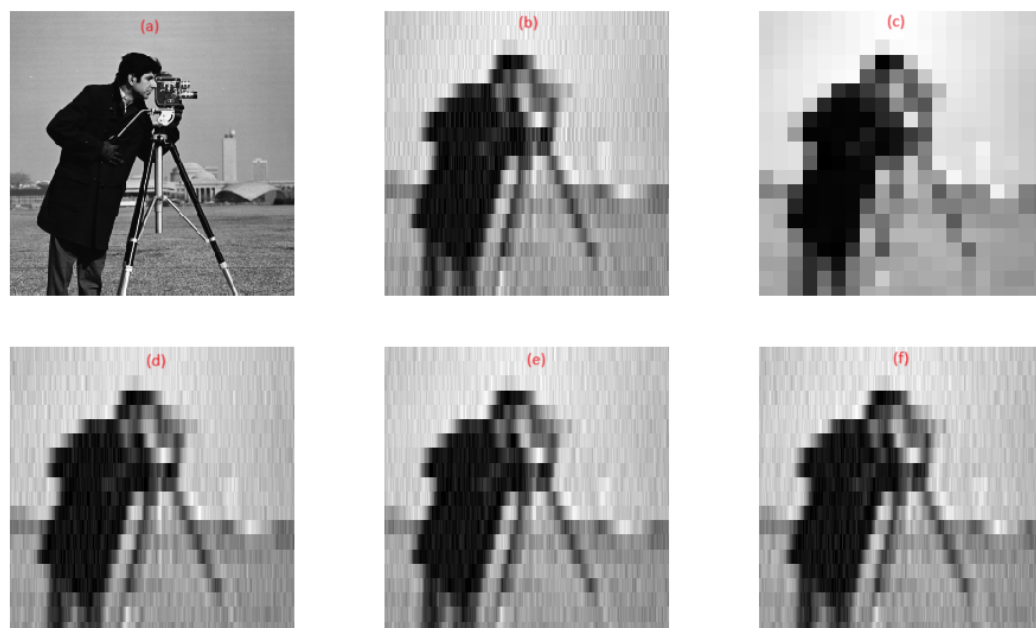


Figure 1. Reconstruction results of the cameraman image with a diffuser having ACL = 13 and various jump values. (a) Original image, (b) jump = 4, (c) jump = 13, (d) jump = 27, (e) jump = 40, and (f) jump = 70.

We see that the heuristic considerations and simulation results are positively correlated, especially for the larger ACL values. In general, when the ACL and jump are co-prime integers it seems that chances are higher to obtain a better reconstruction quality. Intuitively, this can be understood as a way to reduce redundancy in the illumination patterns created by the mask. Importantly, we observe that we can reconstruct an image with jumps that are

smaller than the ACL, which potentially enables us to shorten the diffuser's translation time. More generally, from a certain point on (here it is around jump = 13), further increasing the jump value does not lead to significantly better reconstructions. Below we will show a similar behavior when analyzing our experimental results.

3. Experiment

In order to establish the theoretical work, we performed a complete set of CGI measurements at the NRC Soreq labs. The experimental system involved a typical CGI setup, with a HeNe laser source (632.8 nm, Melles-Griot 25-LHP-991, Carlsbad, CA, USA), a digital micro-mirror device (DMD, VIALUX V-650L, Chemnitz, Germany) creating patterned masks by modulating the beam, and a single-pixel detector (COUNT, Laser Components, Olching, Germany). The DMD is a mega-pixel array of micro-mirrors (10.8 μm size), a controlled subset of which is tilted to determine the spatial modulation of the reflected beam. Similarly to the aforementioned mask or diffuser, the DMD allows CGI, sparing the requirement of a camera to measure the modulated beam pattern. Moreover, the DMD generates repeatable sets of patterns, for accurately comparing the image reconstruction at different jumps of the pattern. Jumps of a diffuser were mimicked by programming an extended matrix and projecting each time a different portion of the matrix by the DMD to emulate the translation induced by the diffuser jump (this was done at 1 kHz). As shown in Figure 2, a structured detection configuration was used for the CGI experiments, with the beam modulated after the object and before being detected. We point out that the masks used in the experiments were completely random and binary, as each pixel (mirror) either reflects the beam towards the detector or away. To vary the ACL, we modified the speckles' sizes each time. The ACLs were produced by defining the number of pixels that construct the randomly positioned speckles (the binning in each speckle dimension). To obtain an equal detected signal in all experimental runs (given that roughly 10% of the DMD pixels were "on"), the number of speckles was designed in accordance with the varying speckle size. We used a ~ 2.5 mm π -shaped metallic object and obtained its image using the aforementioned CGI technique (the image was reconstructed via a simple differential GI [24] algorithm).

We summarize in Figure 3 the CGI reconstruction results, based on a complete set of experimental measurements with different ACL and for varying scanning jumps. Every ACL result is color-coded and presented in a different row of the graph and labeled accordingly. To quantify all the above theoretical predictions, simulation results, and experimental outcomes, we calculated the normalized PSNR (to obtain values between 0 and 1). The curves represent these normalized PSNR values for different jumps, as indicated by the x-axis of the plots. Despite the non-ideal setup and the difference between objects examined in the experiment (a simple π object) and simulation (detailed, more complex images), the experimental results denoted as circles follow roughly the same trend as the theoretical heuristic method (Table 1) and the simulation (Table 2), indicated in Figure 3 by the dashed and solid lines, respectively. Indeed, all these results share several distinctive features, e.g., CGI was successful also for jumps that were smaller than the ACL, and additionally, we see a recurring decrease in the normalized PSNR for jumps that have a common prime factor with the ACL. This supports the above theoretical analysis and shows that judicious choices of the ACL and jump values can improve the reconstruction quality.

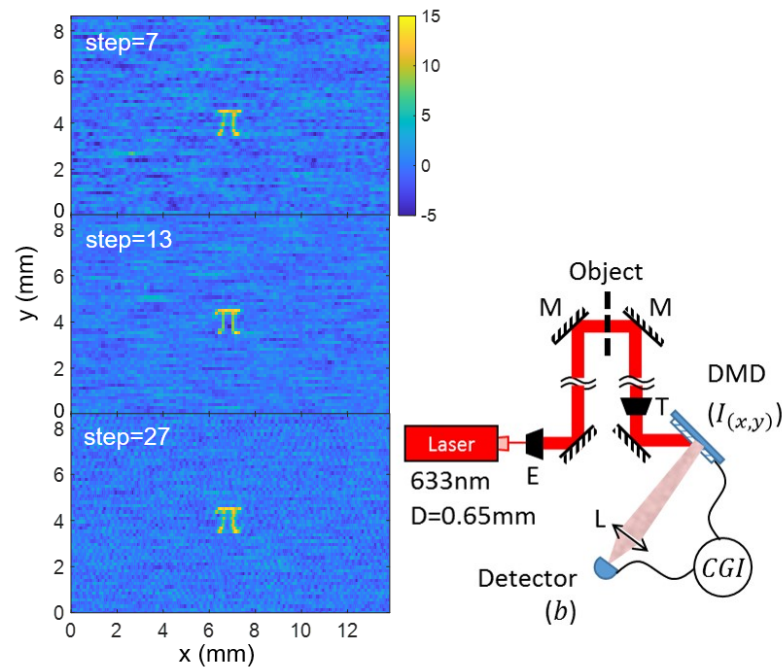


Figure 2. (Right): Our CGI setup in a structured detection configuration, with the beam transmitted through the object located in the far-field (3.3 m). The initial diameter of the beam was $D = 0.65$ mm. Other optical elements include mirrors (M), an expander (E), an imaging telescope (T), a lens (L), and a bucket detector (b). The intensity profile after the DMD is denoted as $I_{(x,y)}$. **(Left):** Reconstructed images of a π -shaped object for $ACL = 13$ and step (jump) sizes of 7, 13, 27. It can be seen that for $step = 13$ the separation between the π legs is slightly worse and the background noise is somewhat greater.

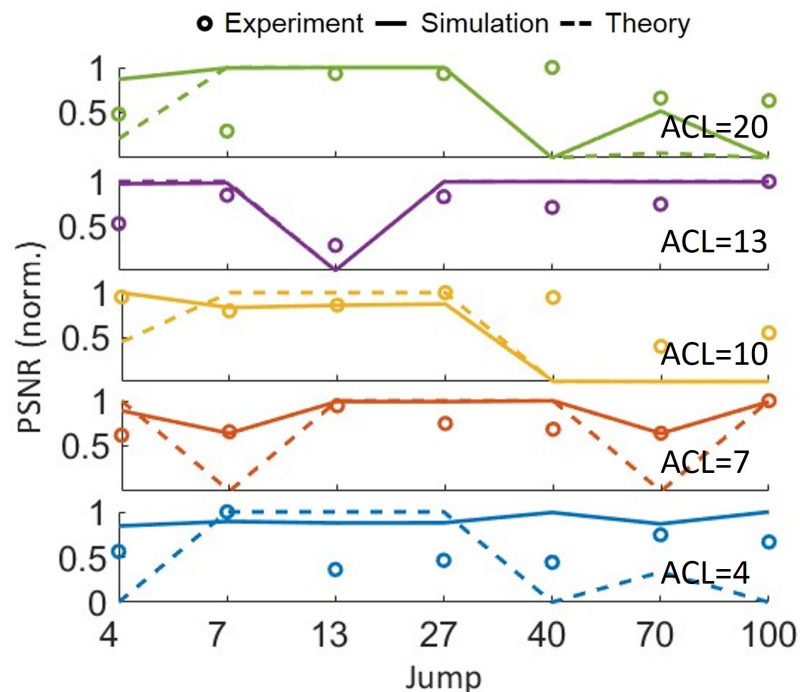


Figure 3. Normalized PSNR obtained in CGI for different ACL values (arising from the different speckle sizes as determined by the DMD) and various sizes of the lateral scan jump of the diffuser. The curves indicate a similar trend in the quality of reconstructed images obtained in the laboratory experiment illustrated in Figure 2, with the computer simulation reported in Table 2 and the theoretical heuristic considerations appearing in Table 1.

4. Conclusions

In this work, we studied both theoretically and experimentally how parameters of the mask (or diffuser) used in computational ghost imaging affect the quality of the reconstructed image. Our results propose some beneficial combinations of the autocorrelation length within the mask and the translation size (the jump parameter used for scanning it). In particular, we see that co-prime values of these parameters are typically advantageous, and moreover, we prove that good reconstructions can be obtained in computational ghost imaging when the jump is relatively small and even smaller than the autocorrelation length. We hope that these findings will lead to more efficient (that is, shorter in time) ghost imaging while also increasing the quality of results in both optical and X-ray applications.

Author Contributions: Conceptualization, Y.A., T.A.-P., S.S. (Sharon Shwartz), and E.C.; methodology, Y.A., T.A.-P., S.S. (Sharon Shwartz), and E.C.; formal analysis, S.S. (Shimon Sukholuski), and O.H.; Experiment: Y.A. and T.A.-P.; writing—original draft preparation, Y.A., S.S. (Shimon Sukholuski), and E.C.; writing—review and editing, Y.A., S.S. (Shimon Sukholuski), O.H., T.A.-P., S.S. (Sharon Shwartz), and E.C.; supervision, T.A.-P., S.S. (Sharon Shwartz), and E.C. All authors have read and agreed to the published version of the manuscript.

Funding: This work was supported by the European Union’s Horizon Europe research and innovation programme under grant agreement No. 101178170, by the Israel Science Foundation under grant agreement No. 2208/24, and by the Pazy Foundation under grant agreement No. 49579.

Data Availability Statement: The original contributions presented in this study are included in the article. Further inquiries can be directed to the corresponding author.

Acknowledgments: We wish to thank Yuval Idan for his assistance in running the simulations.

Conflicts of Interest: The authors declare no conflicts of interest.

References

1. Pittman, T.B.; Shih, Y.; Strekalov, D.; Sergienko, A.V. Optical imaging by means of two-photon quantum entanglement. *Phys. Rev. A* **1995**, *52*, R3429. [[CrossRef](#)] [[PubMed](#)]
2. Bennink, R.S.; Bentley, S.J.; Boyd, R.W. “Two-photon” coincidence imaging with a classical source. *Phys. Rev. Lett.* **2002**, *89*, 113601. [[CrossRef](#)]
3. Gatti, A.; Brambilla, E.; Bache, M.; Lugiato, L.A. Ghost imaging with thermal light: Comparing entanglement and classical correlation. *Phys. Rev. Lett.* **2004**, *93*, 093602. [[PubMed](#)]
4. Shapiro, J.H. Computational ghost imaging. *Phys. Rev. A* **2008**, *78*, 061802. [[CrossRef](#)]
5. Chan, W.L.; Charan, K.; Takhar, D.; Kelly, K.F.; Baraniuk, R.G.; Mittleman, D.M. A single-pixel terahertz imaging system based on compressed sensing. *Appl. Phys. Lett.* **2008**, *93*, 121105. [[CrossRef](#)]
6. Bromberg, Y.; Katz, O.; Silberberg, Y. Ghost imaging with a single detector. *Phys. Rev. A* **2009**, *79*, 053840.
7. Erkmen, B.I. Computational ghost imaging for remote sensing. *J. Opt. Soc. Am. A* **2012**, *29*, 782–789. [[CrossRef](#)]
8. Devaux, F.; Moreau, P.A.; Denis, S.; Lantz, E. Computational temporal ghost imaging. *Optica* **2016**, *3*, 698–701.
9. Le, M.; Wang, G.; Zheng, H.; Liu, J.; Zhou, Y.; Xu, Z. Underwater computational ghost imaging. *Opt. Express* **2017**, *25*, 22859–22868. [[CrossRef](#)]
10. Zhou, C.; Tian, T.; Gao, C.; Gong, W.; Song, L. Multi-resolution progressive computational ghost imaging. *J. Opt.* **2019**, *21*, 055702.
11. Huang, J.; Shi, D.; Meng, W.; Zha, L.; Yuan, K.; Hu, S.; Wang, Y. Spectral encoded computational ghost imaging. *Opt. Commun.* **2020**, *474*, 126105. [[CrossRef](#)]
12. Shimobaba, T.; Endo, Y.; Nishitsuji, T.; Takahashi, T.; Nagahama, Y.; Hasegawa, S.; Sano, M.; Hirayama, R.; Kakue, T.; Shiraki, A.; et al. Computational ghost imaging using deep learning. *Opt. Commun.* **2018**, *413*, 147–151. [[CrossRef](#)]
13. Wang, F.; Wang, H.; Wang, H.; Li, G.; Situ, G. Learning from simulation: An end-to-end deep-learning approach for computational ghost imaging. *Opt. Express* **2019**, *27*, 25560–25572. [[CrossRef](#)]
14. Rizvi, S.; Cao, J.; Zhang, K.; Hao, Q. DeepGhost: Real-time computational ghost imaging via deep learning. *Sci. Rep.* **2020**, *10*, 11400. [[CrossRef](#)] [[PubMed](#)]
15. Pelliccia, D.; Rack, A.; Scheel, M.; Cantelli, V.; Paganin, D.M. Experimental X-ray ghost imaging. *Phys. Rev. Lett.* **2016**, *117*, 113902. [[CrossRef](#)]

16. Schori, A.; Schwartz, S. X-ray ghost imaging with a laboratory source. *Opt. Express* **2017**, *25*, 14822–14828. [[CrossRef](#)]
17. Klein, Y.; Schori, A.; Dolbnya, I.; Sawhney, K.; Schwartz, S. X-ray computational ghost imaging with single-pixel detector. *Opt. Express* **2019**, *27*, 3284–3293. [[CrossRef](#)] [[PubMed](#)]
18. Sefi, O.; Ben Yehuda, A.; Klein, Y.; Sobol, Z.; Bloch, S.; Schwartz, H.; Cohen, E.; Schwartz, S. 20 μm resolution multipixel ghost imaging with high-energy X-rays. *Opt. Express* **2024**, *32*, 37001–37010. [[CrossRef](#)] [[PubMed](#)]
19. Katz, O.; Bromberg, Y.; Silberberg, Y. Compressive ghost imaging. *Appl. Phys. Lett.* **2009**, *95*, 131110. [[CrossRef](#)]
20. Katkovnik, V.; Astola, J. Compressive sensing computational ghost imaging. *J. Opt. Soc. Am. A* **2012**, *29*, 1556–1567. [[CrossRef](#)]
21. Wang, F.; Wang, C.; Chen, M.; Gong, W.; Zhang, Y.; Han, S.; Situ, G. Far-field super-resolution ghost imaging with a deep neural network constraint. *Light Sci. Appl.* **2022**, *11*, 1. [[CrossRef](#)] [[PubMed](#)]
22. Zhang, A.X.; He, Y.H.; Wu, L.A.; Chen, L.M.; Wang, B.B. Tabletop X-ray ghost imaging with ultra-low radiation. *Optica* **2018**, *5*, 374–377. [[CrossRef](#)]
23. Li, C.; Yin, W.; Zhang, Y. User’s guide for TVAL3: TV minimization by augmented lagrangian and alternating direction algorithms. *CAAM Rep.* **2009**, *20*, 4.
24. Ferri, F.; Magatti, D.; Lugiato, L.; Gatti, A. Differential ghost imaging. *Phys. Rev. Lett.* **2010**, *104*, 253603. [[CrossRef](#)]

Disclaimer/Publisher’s Note: The statements, opinions and data contained in all publications are solely those of the individual author(s) and contributor(s) and not of MDPI and/or the editor(s). MDPI and/or the editor(s) disclaim responsibility for any injury to people or property resulting from any ideas, methods, instructions or products referred to in the content.